Wave-averaged motion of small particles in surface gravity waves: Effect of particle shape on orientation, drift, and dispersion

Nimish Pujara 1,* and Jean-Luc Thiffeault 2,†

²Department of Mathematics, University of Wisconsin–Madison, Madison, Wisconsin 53706, USA



(Received 2 April 2023; accepted 30 June 2023; published 26 July 2023)

Particles such as microplastics and phytoplankton suspended in the water column in the natural environment are often subject to the action of surface gravity waves. By modeling such anisotropic particles as small spheroids that slowly settle (or rise) in a wavy environment, we consider how the particle shape and buoyancy couple to the background wave-driven flow to influence the particle orientation, drift, and dispersion. A multiscale expansion allows the wave-induced oscillations to be separated from the wave-averaged particle motion. Using the wave-averaged equations of particle motion, we demonstrate that spheroidal particles have a wave-induced preferential orientation with different stable solutions for prolate and oblate particles. The resulting preferential orientation positions particles with their longest axis pointing in the direction of wave propagation and upwards against gravity. The angle at which the longest axis points upwards is a function of particle aspect ratio. In this orientation, particles drift in the direction opposite to wave propagation, weakening and potentially even reversing their Stokes drift. The wave-induced stable orientation also results in a reduced settling velocity relative to a random (isotropic) orientation. The dispersion of a particle cloud is controlled by the distribution of orientations. For a cloud of particles released together with random (isotropic) orientation, the initial cloud growth rate is ballistic in all directions. Wave action acts to suppress the vertical dispersion but enhances horizontal dispersion into a super-ballistic state when the Stokes drift shear acts on a particle cloud that has expanded in the vertical direction.

DOI: 10.1103/PhysRevFluids.8.074801

I. INTRODUCTION

The motion of particles within flow driven by surface gravity waves is related to the transport of abiotic (sediment, marine debris including oil droplets, macroplastics, and microplastics) and biotic (plankton, organic aggregates) particles in coastal and ocean environments. Motivated by this wide array of applications, recent research on this topic has investigated wave-induced drift of spherical particles [1–10], preferential orientation and transport of anisotropic particles [11–16], and behavior of active particles such as planktonic microswimmers [16–20].

Here we consider particle transport in waves and focus on two interrelated factors: particle buoyancy and particle shape. These are coupled since particle orientation influences transport via orientation-dependent drag forces. The simplest approach to including the effect of both shape and buoyancy is to model particles in the inertialess limit as spheroids that settle (or rise) in the water column for small particles whose density is not too far from the fluid density. A number

¹Department of Civil and Environmental Engineering, University of Wisconsin–Madison, Madison, Wisconsin 53706, USA

^{*}npujara@wisc.edu

[†]jeanluc@math.wisc.edu

of applications fall within these assumptions (e.g., microplastics, phytoplankton), justifying this approach.

We consider slowly settling (or rising) spheroidal particles immersed in a flow driven by smallamplitude progressive waves. We first derive formulas for wave-averaged translation and rotation using a multiscale expansion (Sec. II) and then discuss the mutual interactions between particle orientation and transport via analysis and numerical solution of the wave-averaged formulas (Sec. III). Extending and correcting previous results of wave-induced preferential orientations [11,12], we find that the wave-averaged orientation dynamics of spheroids have up to six fixed points in the phase space spanned by their polar angles (corresponding to three distinct physical orientations), but only one of these fixed points (and orientations) is stable. The stable fixed point represents the wave-induced preferential orientation of the particle and is only a function of the particle aspect ratio (and not a function of wave amplitude or frequency) as previously found; however, we show that the stable fixed points for oblate and prolate shapes are on different branches of solution, so that the longest particle axis always has a component in the direction of wave propagation and upwards against gravity. Considering the effect of particle shape on drift, we find that the drift due to particle orientation always acts in the direction opposite to wave propagation (and Stokes drift) in the horizontal direction, and vertical settling is always reduced compared to an equivalently sized sphere or random (isotropic) orientation. Finally, we consider the effect of waves on particle dispersion, which is controlled by the distribution of particle orientations. For an initially isotropic distribution of orientations, we provide analytical predictions for the ballistic growth rate of particle clouds before the effect of waves begins to alter particle orientation. As the effects of wave-induced reorientation accumulate, the vertical dispersion rate weakens. However, the dispersion rate in the horizontal direction grows because the shear of the Stokes drift acts on the particle cloud as it expands in the vertical direction, resulting in a period of superballistic dispersion. We end with a summary and discussion on the limitations and extensions of our results (Sec. IV).

II. WAVE-AVERAGED PARTICLE MOTION

We consider small-amplitude, two-dimensional progressive surface gravity waves as described by $\eta = ka\cos(x - t)$, where the fluid velocity field is given by

$$u_{x} = \varepsilon_{w} c(z) \cos(x - t), \tag{1a}$$

$$u_z = \varepsilon_{\rm w} \, {\rm s}(z) \sin(x-t), \tag{1b}$$

where

$$c(z) = \cosh(z + kh)/\cosh kh, \quad s(z) = \sinh(z + kh)/\cosh kh. \tag{2}$$

Here a is the wave amplitude, k is the wave number, and ω is the angular frequency. The freesurface position is $z = \eta$ and the fluid velocity field is $\mathbf{u} = [u_x, u_z]$. The small-amplitude condition requires that $\varepsilon_w = ka/\tanh kh \ll 1$, and the dispersion relation is given by $\omega^2 = gk \tanh kh$. In terms of velocity gradients, the flow is irrotational $(\mathbf{\Omega} = \frac{1}{2}[\nabla \mathbf{u} - (\nabla \mathbf{u})^T] \equiv 0)$, and the components of the strain rate tensor $(\mathbf{S} = \frac{1}{2}[\nabla \mathbf{u} + (\nabla \mathbf{u})^T])$ are given by

$$S_{xx} = -S_{zz} = -\varepsilon_{w} c(z) \sin(x - t), \qquad (3a)$$

$$S_{xz} = S_{zx} = \varepsilon_{w} s(z) \cos(x - t).$$
 (3b)

We have used the dimensionless variables $t \to \omega t$, $x \to kx$, $u \to u/(\omega/k)$. Figure 1 shows the velocity field and the velocity gradients in a wave-driven flow field.

We consider the motion of small, slowly settling (or rising) spheroids described by

$$\boldsymbol{v} = \boldsymbol{u} + \boldsymbol{w}; \quad \boldsymbol{w} = -v_{S\perp} \boldsymbol{e}_{z} - (v_{S\parallel} - v_{S\perp})(\boldsymbol{e}_{z} \cdot \boldsymbol{p})\boldsymbol{p}, \tag{4a}$$

$$\dot{\mathbf{p}} = \mathbf{\Omega} \, \mathbf{p} + \lambda [\mathbf{S} \mathbf{p} - (\mathbf{p}^T \mathbf{S} \, \mathbf{p}) \mathbf{p}], \tag{4b}$$

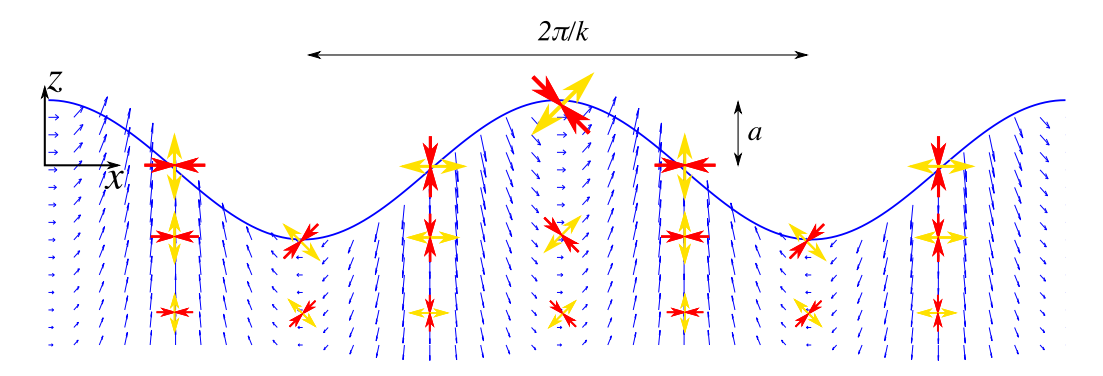


FIG. 1. Small-amplitude surface gravity waves traveling in the positive *x* direction with the velocity field (smaller blue arrows) and velocity gradients (larger red and yellow arrows).

where the particle velocity v is taken to be the sum of the local fluid velocity u and the settling velocity w, and the particle rotation—defined by the rate of change of a unit vector p that points along the particle's symmetry axis—is given by Jeffery's equations [21]. The particle shape is defined by $\lambda \in [-1, 1]$ and is related to the particle aspect ratio AR via $\lambda = (AR^2 - 1)/(AR^2 + 1)$. In the expression for the settling velocity vector, $v_{s\parallel}$ is the settling velocity in quiescent fluid with the symmetry axis parallel to gravity, and $v_{s\perp}$ is the same with the symmetry axis perpendicular to gravity. These equations have been made dimensionless with the same scales as the fluid velocity field. Equations (4) assume that the particles are small, moving slowly relative to the fluid such that the Reynolds and Stokes numbers of their relative translation and rotation is negligibly small, and thus their dynamics can be considered inertialess and solved within the context of Stokes flow (see Chs. 1–3 in Ref. [22] for a discussion of the physics involved). While this particle model is well established, we provide a summary of the derivation for the particle settling vector w in Appendix A for convenience.

Using polar angles ϕ and θ that are both defined between 0 and π (Fig. 2), the components of the particle orientation vector can be written as [16]

$$p_x = \sin \phi \sin \theta, \quad p_y = \cos \theta, \quad p_z = \cos \phi \sin \theta.$$
 (5)

The particle equations (4) can be rewritten as the following component-wise ODEs by using (1), (3), and (5) [12,16]:

$$\dot{x} = \varepsilon_{\rm w} \, c(z) \cos(x - t) - (v_{\rm s\parallel} - v_{\rm s\perp}) \cos \phi \sin \phi \sin^2 \theta, \tag{6a}$$

$$\dot{y} = -(v_{s\parallel} - v_{s\perp})\cos\phi\cos\theta\sin\theta,\tag{6b}$$

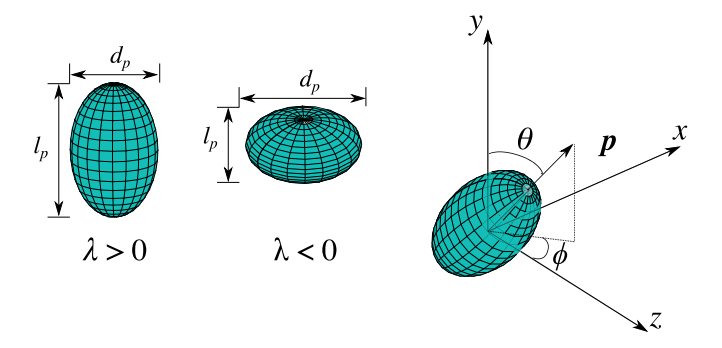


FIG. 2. Spheroids with aspect ratios AR = ℓ_p/d_p and the angles ϕ and θ defining the orientation.

$$\dot{z} = \varepsilon_{\rm W} \,\mathrm{s}(z) \sin(x-t) - v_{\rm s\perp} - (v_{\rm s\parallel} - v_{\rm s\perp}) \cos^2 \phi \,\sin^2 \theta, \tag{6c}$$

$$\dot{\phi} = \lambda \, \varepsilon_{\rm w} \left[s(z) \cos (x - t) \cos 2\phi - c(z) \sin (x - t) \sin 2\phi \right], \tag{6d}$$

$$\dot{\theta} = \lambda \, \varepsilon_{\rm w} \left[s(z) \cos (x - t) \sin 2\phi + c(z) \sin (x - t) \cos 2\phi \right] \sin \theta \cos \theta. \tag{6e}$$

To derive the wave-averaged motions, we use a two-time expansion of the particle position and orientation to isolate the fast (wave-induced oscillations) motions from the slow (wave-averaged) motions [10,16]:

$$\begin{bmatrix} \mathbf{x}(t) \\ \phi(t) \\ \theta(t) \end{bmatrix} = \begin{bmatrix} \mathbf{X}(T) + \epsilon \, \mathbf{x}_1(t, T; \epsilon) + \cdots \\ \Phi(T) + \epsilon \, \phi_1(t, T; \epsilon) + \cdots \\ \Theta(T) + \epsilon \, \theta_1(t, T; \epsilon) + \cdots \end{bmatrix}, \quad T = \epsilon^2 t,$$

where ϵ is a small quantity that acts as an ordering parameter. Since the fluid velocity is $u \sim O(\varepsilon_w)$, which is a small quantity, it is rescaled in the expansion as $\varepsilon_w \to \epsilon \varepsilon_w$. For the particle velocity, we are investigating the dynamics of small particles that settle slowly through the flow, and hence the particle settling velocity is rescaled as an order smaller than the fluid velocity, $v_s \to \epsilon^2 v_s$. Substituting the expansion and scalings into (6) and collecting terms gives the appropriate equations of motion at each order. This procedure is given in full in Appendix B. Here we quote only the main result, which is the wave-averaged particle motion at the slow timescale:

$$\partial_T X = \varepsilon_w^2 C(Z) - (v_{s\parallel} - v_{s\perp}) \cos \Phi \sin \Phi \sin^2 \Theta, \tag{7a}$$

$$\partial_T Y = -(v_{s\parallel} - v_{s\perp})\cos\Phi\sin\Theta\cos\Theta,\tag{7b}$$

$$\partial_T Z = -[v_{s\perp} + (v_{s\parallel} - v_{s\perp})\cos^2\Phi\sin^2\Theta],\tag{7c}$$

$$\partial_T \Phi = \lambda \varepsilon_w^2 S(Z)(\lambda + \cos 2\Phi), \tag{7d}$$

$$\partial_T \Theta = \lambda \varepsilon_w^2 S(Z) \sin 2\Phi \sin \Theta \cos \Theta. \tag{7e}$$

where

$$C(Z) = \frac{\cosh 2(Z + kh)}{2\cosh^2 kh}, \quad S(Z) = \frac{\sinh 2(Z + kh)}{2\cosh^2 kh}.$$
 (8)

The effects of particle orientation on its drift appear with the coefficient $(v_{s\parallel}-v_{s\perp})$, which is the difference between the settling velocities when the particle symmetry axis is parallel to gravity and perpendicular to gravity. This quantity is positive for prolate particles $(\lambda > 0)$ and negative for oblate particles $(\lambda < 0)$.

To directly compare the wave-averaged dynamics (7) against the full dynamics (6), it is also important to correctly transform the initial conditions (cf. [10,16]), as also detailed in Appendix B.

III. ANALYSIS OF PARTICLE MOTION

A. Orientation

The $\partial_T \Phi$ equation (7d) shows there are fixed points in the Φ dynamics that satisfy $\lambda + \cos 2\Phi = 0$, which are functions only of the particle shape and independent of all other variables (see also [12,16]). The critical angles corresponding to the two fixed points are

$$\Phi_1^{\text{crit}} = \frac{1}{2}\arccos(-\lambda) \in [0, \pi/2], \quad \Phi_2^{\text{crit}} = \pi - \Phi_1^{\text{crit}} \in [\pi/2, \pi].$$
(9)

The 3D orientational dynamics can be isolated from the translational dynamics by taking the ratio of $\partial_T \Phi$ and $\partial_T \Theta$ in (7):

$$\frac{d\Phi}{d\Theta} = \frac{2(\lambda + \cos 2\Phi)}{\sin 2\Phi \sin 2\Theta}.$$
 (10)

This shows that the orientational dynamics are independent of whether and how the particles move relative to the flow (e.g., sinking, swimming, rising) and independent of all variables except the

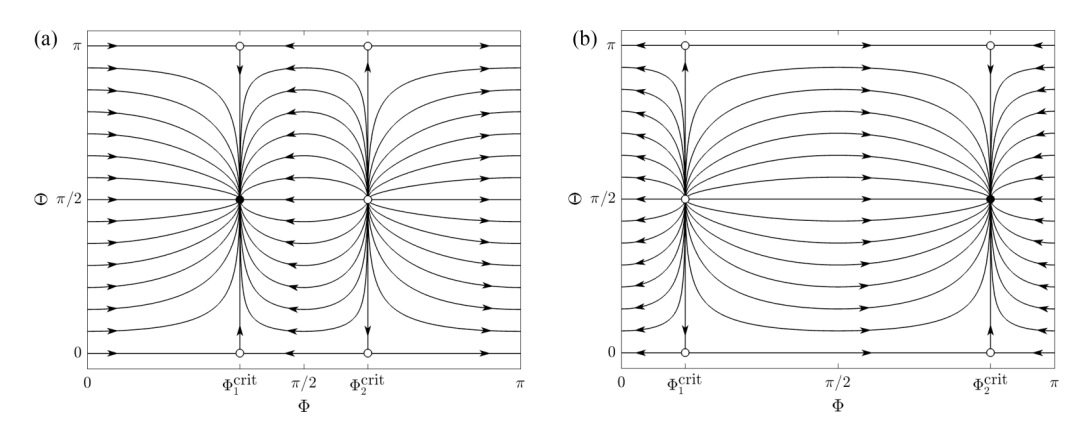


FIG. 3. Φ - Θ phase portrait with (a) $\lambda = 0.6$ and (b) $\lambda = -0.6$.

particle shape, even when we include out-of-plane rotations. This equation was previously reported for spheroidal microswimmers in waves [16], where the following solution was also provided:

$$\sin\Theta = \left(1 + \cot^2\Theta(0) \frac{|\lambda + \cos 2\Phi|}{|\lambda + \cos 2\Phi(0)|}\right)^{-1/2} \tag{11}$$

for initial conditions $\Phi(0)$ and $\Theta(0)$. Figure 3 shows phase portraits corresponding to this solution. We observe that there are fixed points at $(\Phi,\Theta)=(\Phi_1^{crit},0), (\Phi_1^{crit},\pi/2), (\Phi_1^{crit},\pi)$ and $(\Phi,\Theta)=(\Phi_2^{crit},0), (\Phi_2^{crit},\pi/2), (\Phi_2^{crit},\pi)$, which correspond to three distinct physical orientations; however, only one of the three orientations is stable. For prolate particles $(\lambda>0)$, the stable fixed point is $(\Phi,\Theta)=(\Phi_2^{crit},\pi/2)$ whereas for oblate particles $(\lambda<0)$, it is $(\Phi,\Theta)=(\Phi_2^{crit},\pi/2)$.

This conclusion can be shown to hold for all shapes $(-1 \le \lambda \le 1)$ with a formal stability analysis of the fixed points. Writing small perturbations in Φ and Θ about the fixed points as

$$\Phi = \Phi^{\text{crit}} + \varphi, \quad \Theta = \frac{1}{2}\pi + \vartheta,$$

we obtain the linearized system

$$\begin{bmatrix} \dot{\varphi} \\ \dot{\vartheta} \end{bmatrix} = A \begin{bmatrix} \varphi \\ \vartheta \end{bmatrix} \quad \text{where} \quad A = \varepsilon_{\rm w}^2 \, S(Z) \, \lambda \begin{bmatrix} -2\sin 2\Phi^{\rm crit} & 0 \\ 0 & -\sin 2\Phi^{\rm crit} \end{bmatrix}. \tag{12}$$

For simplicity, we have assumed that Z is a constant for the stability analysis, which is equivalent to considering neutrally buoyant particles. The trace and determinant of A are given by

$$\operatorname{Tr} A = -3\lambda \varepsilon_{\mathrm{w}}^{2} \operatorname{S}(Z) \sin 2\Phi^{\mathrm{crit}}, \quad \det A = 2\lambda^{2} \varepsilon_{\mathrm{w}}^{4} \operatorname{S}^{2}(Z) \sin^{2} 2\Phi^{\mathrm{crit}}.$$

From this, we can confirm that $\det A>0$ and $(\operatorname{Tr} A)^2-4\det A>0$ for all nonspherical shapes, and thus the fixed points are either stable or unstable nodes. Considering the sign of $\operatorname{Tr} A$ for $\Phi^{\operatorname{crit}}\in\{\Phi_1^{\operatorname{crit}},\Phi_2^{\operatorname{crit}}\}$ shows that $(\Phi=\Phi_1^{\operatorname{crit}},\Theta=\pi/2)$ is a stable node for $\lambda>0$ and an unstable node for $\lambda<0$. Conversely, $(\Phi=\Phi_2^{\operatorname{crit}},\Theta=\pi/2)$ is an unstable node for $\lambda>0$ and a stable node for $\lambda<0$. These findings are consistent with the phase portraits in Fig. 3.

Since there is one globally attractive fixed point with $\Theta = \pi/2$, we can conclude that particles of all shapes will eventually reach this fixed point and thus align their axis of symmetry within the flow plane. Figure 4 shows the the critical angles Φ_i^{crit} as a function of particle shape λ for orientation p in the x-z plane; stable regions are shown in black. Physically, the stable orientation for all shapes is one where the particle's longest dimension is pointing in the wave propagation direction and upwards against gravity (see insets in Fig. 4). This can be understood as the shape-dependent response of the particle to the Lagrangian strain (i.e., the strain-rate integrated along a particle trajectory). As the difference between Lagrangian and Eulerian wave averages, the stable orientation is analogous to the classical Stokes drift, and it appears as such in the wave-averaged equations (7).

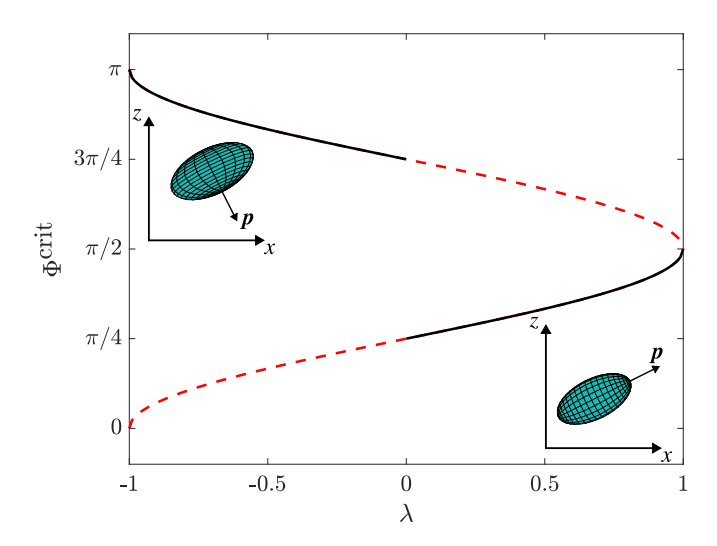


FIG. 4. Critical angles Φ^{crit} as given by Eq. (9). The solid black curves show the stable region, whereas the dashed red curves show the unstable region. The insets show the stable orientation for $\lambda = \pm 0.6$.

While the stable orientation is only a function of the particle shape, the rate at which this orientation is achieved is a function of both the particle shape and the waves. The coefficient $\lambda \varepsilon_w^2 S(Z)$, which appears in Eqs. (7d) and (7e), controls this rate. Thus, a higher aspect ratio particle, larger wave amplitude, and higher position in the water column all result in the particle reaching its stable orientation faster.

Previous efforts have analyzed the preferential orientations [11,12]. Our analysis agrees with theirs for prolate particles (i.e., the stable orientation is $\Phi = \Phi_1^{crit}$, $\Theta = \pi/2$ for $\lambda > 0$), but we find that the stable orientation of oblate particles is different (i.e., the stable orientation is $\Phi = \Phi_2^{crit} = \pi - \Phi_1^{crit}$, $\Theta = \pi/2$ for $\lambda < 0$). While they analyzed the preferential orientations using wave-resolved equations, the wave-averaged formulation applied here considerably simplifies matters since the preferential orientations become fixed points rather than limit cycles. In the wave-averaged systems, it is clear that different solution branches are stable for oblate and prolate particles, respectively.

While Φ tends towards its stable fixed point in the wave-averaged motion, the unaveraged solution ϕ includes an oscillatory component. We can predict the leading order amplitude and phase lag of these oscillations using the $O(\epsilon^1)$ solutions. In particular, we expect that $\phi = \Phi + A_\phi \cos(X - t + L_\phi) + O(\epsilon^2)$ where A_ϕ is the amplitude of oscillation and L_ϕ is the phase lag relative to the waves. From Eq. (B3), we find

$$A_{\phi} = \pm \frac{\epsilon_{\rm w}}{\cosh kh} \lambda \sqrt{\sinh^2(Z + kh) + \sin^2 2\Phi}, \tag{13a}$$

$$L_{\phi} = \arctan\left[-\frac{\tanh(Z+kh)}{\tan 2\Phi}\right]. \tag{13b}$$

These expressions are valid for particles with time-varying wave-averaged vertical position (due to sinking, rising, swimming, etc.) since those dynamics are included in the value of Z(T).

Figure 5 shows how the solution $\phi \approx \Phi + A_{\phi} \cos(X - t + L_{\phi})$ correctly tracks the evolution of ϕ computed numerically and how the solution for Φ tends towards its stable fixed point. From Eq. (13), we can also see that the amplitude of the angular oscillations are larger for larger wave amplitude, increased nonsphericity, and when the particle is closer to the surface. For passive neutrally buoyant particles whose wave-averaged vertical position remains unchanged, A_{ϕ} and L_{ϕ} become constants

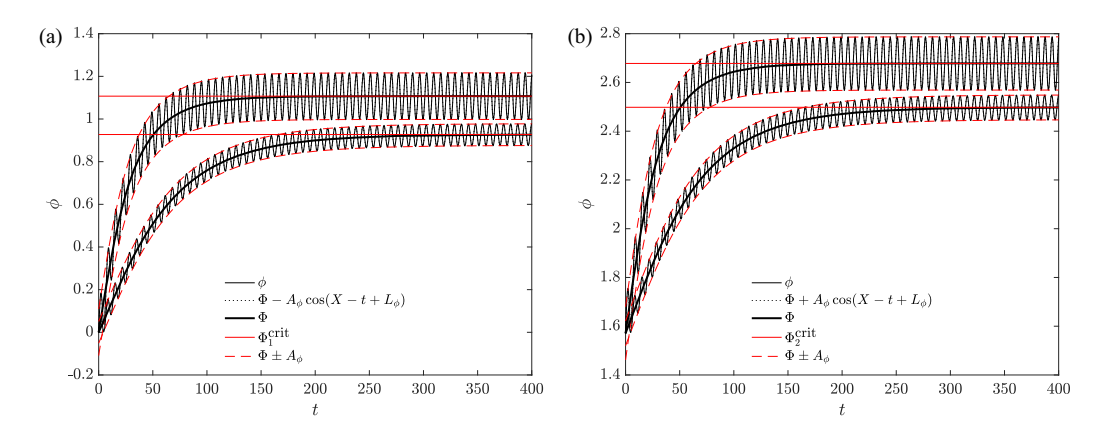


FIG. 5. Evolution of ϕ with Z=-0.10, ka=0.2, and kh=40 for (a) prolate shapes ($\lambda=0.6$ for upper curves, $\lambda=0.28$ for lower curves) and (b) oblate shapes ($\lambda=-0.6$ for upper curves, $\lambda=-0.28$ for lower curves). The curves for ϕ and Φ are obtained from numerical solutions, A_{ϕ} and L_{ϕ} are obtained from Eq. (13), and $\Phi^{\rm crit}$ are obtained from Eq. (9). An initial condition correction (B6) is used to directly compare $\phi(t)$ and $\Phi(t)$.

when Φ reaches its stable fixed point. In fact, in deep water (large kh) where the particle is near the surface (small Z), the above expressions simplify considerably to

$$A_{\phi} = \pm \lambda k a,\tag{14a}$$

$$L_{\phi} = \begin{cases} -\frac{\pi}{2} + 2\Phi, & 0 < \Phi < \frac{\pi}{2}, \\ \frac{\pi}{2} + 2\Phi, & \frac{\pi}{2} < \Phi < \pi. \end{cases}$$
 (14b)

Thus, the orientation oscillation amplitude is larger for higher aspect ratio particles and steeper waves, and the phase lag evolves with the wave-averaged orientation. In their stable orientations, high-aspect-ratio prolate particles (fibers) oscillate with no phase lag whereas high-aspect-ratio oblate particles (disks) oscillate with a phase lag of $\frac{\pi}{2}$.

B. Drift

From (7), we define the horizontal and vertical drift velocities

$$v_X = \partial_T X = u_{\text{SD}} - \frac{1}{2} (v_{\text{s}\parallel} - v_{\text{s}\perp}) \sin 2\Phi \sin^2 \Theta, \tag{15a}$$

$$v_Z = \partial_T Z = -[v_{s\perp} + (v_{s\parallel} - v_{s\perp})\cos^2 \Phi], \tag{15b}$$

where the Stokes drift $u_{SD} = \varepsilon_w^2 C(Z)$ is solely a function of the waves and the second term is solely a function of the particle as it behaves in waves. Substituting a particle's settling velocities $(v_{s\parallel}, v_{s\perp})$ and stable orientation angles $(\Phi_{\text{stable}}^{\text{crit}}, \Theta_{\text{stable}}^{\text{crit}})$ into (15) gives its wave-induced drifts.

Examining the horizontal component, we see that particle anisotropy always leads to a negative value for the second term on the right side of (15a). While $\sin^2\Theta_{\text{stable}}^{\text{crit}}=1$ for all particles, $(v_{\text{s}\parallel}-v_{\text{s}\perp})>0$ and $\sin2\Phi_{\text{stable}}^{\text{crit}}>0$ for prolate particles and $(v_{\text{s}\parallel}-v_{\text{s}\perp})<0$ and $\sin2\Phi_{\text{stable}}^{\text{crit}}<0$ for oblate particles. This means that the wave-induced particle drift is reduced compared with the Stokes drift or can even be in the opposite direction.

The effects of particle shape on horizontal drift are isolated in Fig. 6(a) by normalizing the second term on the right side of (15a) by the settling velocity of a volume-matched sphere $v_{Z,\text{sphere}}$ (A7). The largest reduction in horizontal drift velocity is for moderately anisotropic shapes. An alternative way to observe the altered horizontal drift is to consider the horizontal drift as a fraction of the Stokes drift, $v_X/u_{\text{SD}} = 1 - \frac{1}{2}((v_{\text{s}\parallel} - v_{\text{s}\perp})/u_{\text{SD}})\sin 2\Phi \sin^2\Theta$. Since the settling velocity and the Stokes drift are both second-order quantities, the second term is O(1) showing that the horizontal

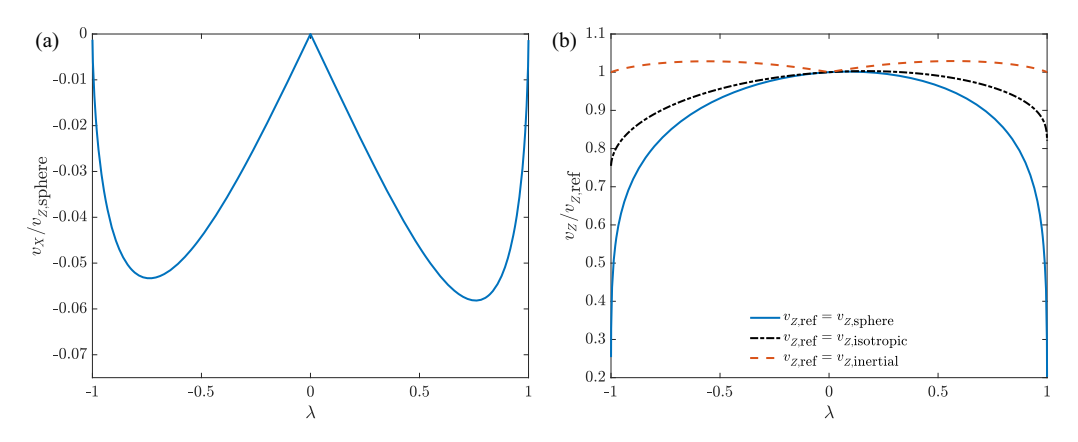


FIG. 6. Effect of particle shape and wave-induced orientation on horizontal and vertical drift velocities.

drift can be significantly altered from the classical Stokes drift. To see that the particle motion can be in the opposite direction to the Stokes drift, consider also that the Stokes drift weakens quickly with depth, whereas the horizontal drift due to preferential orientation doesn't. Thus, the horizontal drift due to preferential orientation overcomes the Stokes drift at some point for all settling particles. After particles sink below the influence of the wave-induced velocity field, they will continue to drift in the negative *x* direction if left undisturbed.

For the vertical drift component, the influence of particle anisotropy can be quantified by comparing the wave-induced settling velocity against three different limits: (1) the settling of a volume-matched sphere $v_{Z,\text{sphere}}$ (A7); (2) the settling of the same particle, but in a random (isotropic) orientation $v_{Z,\text{isotropic}} = (2v_{s\perp} + v_{s\parallel})/3$ where Φ is distributed uniformly in $[0, \pi]$ and $\cos \Theta$ is distributed uniformly in [-1, 1]; and (3) the settling of the same particle, but in the orientation resulting from inertial particle torques that minimize the settling velocity $v_{Z,\text{inertial}} = \min(v_{s\perp}, v_{s\parallel})$. While limit (1) captures the effect of particle shape and orientation for a given volume, limits (2) and (3) capture the effect of particle orientation for a given shape and volume. Figure 6(b) shows these comparisons. We observe that using random (isotropic) orientation or volume-equivalent spheres can vastly overpredict the settling velocity of spheroids in waves, while using the settling velocity spheroids in their inertial orientations results in only a small error.

C. Dispersion

The particle drift velocities (7a)–(7c) are functions of Z, Φ , and Θ . Thus, trajectories of particles with the same shape and size that are released with differences in initial vertical position and/or differences in initial orientation will diverge. Here we focus on particle dispersion due to differences in initial orientation.

A useful limit to consider for particle dispersion due to orientation effects is the dispersion of particles of a given shape, with random (isotropic) orientations, settling in quiescent fluid. In this case the variance of the horizontal and vertical drifts can be calculated as the centralised second moments of v_X and v_Z with Φ distributed uniformly in $[0, \pi]$ and $\cos \Theta$ distributed uniformly in [-1, 1]. This gives variances

$$\operatorname{var}(v_X)_{\text{isotropic}} = \frac{1}{15}(v_{\text{s}\parallel} - v_{\text{s}\perp})^2 \to \operatorname{var}(X)_{\text{isotropic}} = \frac{1}{15}(v_{\text{s}\parallel} - v_{\text{s}\perp})^2 t^2, \tag{16a}$$

$$\operatorname{var}(v_Z)_{\text{isotropic}} = \frac{4}{45}(v_{s\parallel} - v_{s\perp})^2 \to \operatorname{var}(Z)_{\text{isotropic}} = \frac{4}{45}(v_{s\parallel} - v_{s\perp})^2 t^2. \tag{16b}$$

Equation (16) shows that particle dispersion due to random orientation is in the ballistic regime where the size of the particle cloud grows as $\sim t$ (in contrast to a diffusive regime where the cloud size would grow as $\sim t^{1/2}$). It also shows that the particle cloud size will grow faster in the vertical

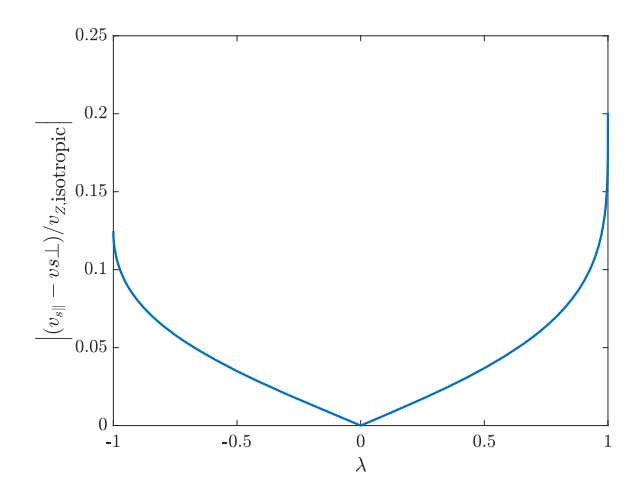


FIG. 7. Scaling for particle cloud growth rate per unit vertical distance of settling (or rising) for different shapes that begin (and remain) in random (isotropic) orientation. The actual growth rate of the particle cloud size will be some multiple of the quantity shown.

direction compared with the horizontal direction. Using the mean particle settling velocity for random (isotropic) orientations ($v_{Z,isotropic} = (2v_{s\perp} + v_{s\parallel})/3$), we can convert time to distance from initial location $t = -(Z - Z_0)/v_{Z,isotropic}$ and find the variance of the particle cloud as a function of depth:

$$var(X)_{isotropic} = \frac{9}{15} \left[\frac{v_{s\parallel} - v_{s\perp}}{2v_{s\perp} + v_{s\parallel}} (Z - Z_0) \right]^2, \quad var(Z)_{isotropic} = \frac{4}{5} \left[\frac{v_{s\parallel} - v_{s\perp}}{2v_{s\perp} + v_{s\parallel}} (Z - Z_0) \right]^2. \quad (17)$$

Since the cloud size can be characterized by the standard deviation of particle positions, the cloud size is expected to grow with depth as $\sim |(v_{s\parallel} - v_{s\perp})/v_{Z,isotropic}|$ per unit vertical distance that the cloud travels. Figure 7 shows this function, which depends on only particle shape. We observe that the dispersion rate increases for more anisotropic particle shapes, which is due to the increased drag anisotropy. We also see that highly elongated shapes (fibers) have a higher dispersion rate per unit vertical drop than highly flattened shapes (disks).

To understand how particle shape affects dispersion, we analyze a cloud of particles of a given shape and size that are released together with random (isotropic) orientations at the water surface. Figure 8 shows the dispersion of particles initialized at X = Y = Z = 0 with an isotropic distribution. These simulations cover $\varepsilon_w \in [0.1, 0.3], \lambda \in [-0.99, 0.99], \text{ and } v_{Z, \text{isotropic}} \in [0.001, 0.01].$ The particle cloud initially disperses at a rate predicted by (16) and (17), but this dispersion rate is modified by two factors: (1) the particle drift velocities start to converge as the particle orientation distribution converges towards the wave-induced preferential orientation, reducing the dispersion rate in both directions; and (2) the vertical variation in Stokes drift begins to shear the cloud horizontally as the particle cloud grows in the vertical direction, increasing its dispersion rate in the wave direction. Figure 9 shows particle cloud snapshots at different times to illustrate this behavior. Both vertical and horizontal dispersion are initially ballistic (particle position variance $\sim t^2$), but the vertical dispersion becomes subballistic and continues to decrease until the particles fall below the influence of wave motion, whereas the initial vertical dispersion allows the horizontal dispersion to become temporarily superballistic before decreasing back towards an intermediate growth rate. The superballistic regime is notable since it may contribute to the very high rates of horizontal spreading near the water surface. Note that the behavior seen in Fig. 9 would not be observed for spherical particles; spheres with a similar initial configuration would show no dispersion because their drift velocities are only functions of initial wave-averaged vertical position. For completeness,

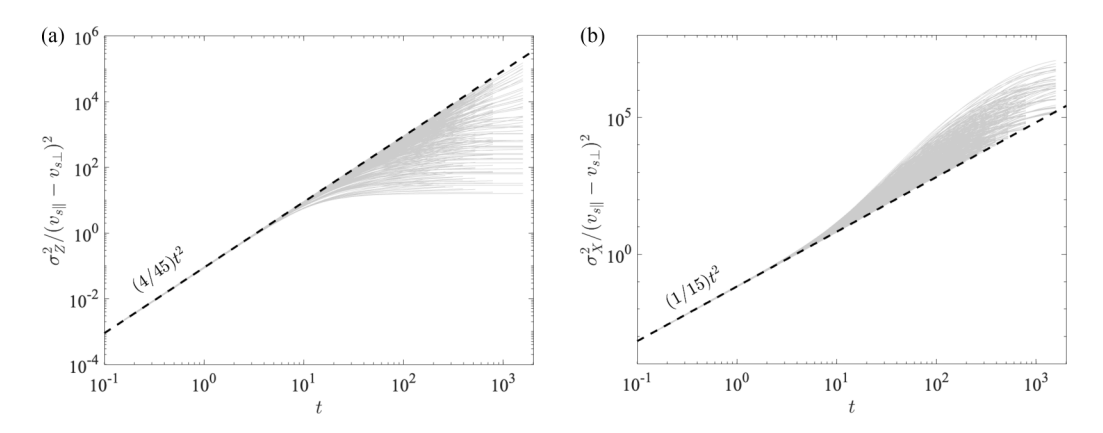


FIG. 8. Particle dispersion (quantified by variance of particle position) as a function of time: (a) vertical dispersion and (b) horizontal dispersion in the wave propagation direction. Thin gray lines show numerical simulations that span $\varepsilon_{\rm w} \in [0.1, 0.3]$, $\lambda \in [-0.99, 0.99]$, and $v_{\rm Z,isotropic} \in [0.001, 0.01]$. Thick dashed lines are the initial dispersion rates in Eq. (16).

note that the vertical variation in the Stokes drift (the Stokes drift shear) also affects the orientation dynamics, but at higher order than the wave-averaged preferential orientation (B5), and thus this effect is small.

While we have quantified the dispersion of particles of a given shape initiated at different orientations, there are at least two other mechanisms by which particles can disperse: (1) since particle drifts are functions of particle shape and size, we can expect that particles of different shapes and sizes released together will disperse; and (2) since Stokes drift is very sensitive to the initial wave-averaged vertical position, even small $[O(\varepsilon_{\rm w}^2)]$ variations in the initial condition will produce horizontal dispersion of particle clouds (Fig. 5 in Ref. [10]). The relative importance of the different mechanisms is not examined here and left for future work.

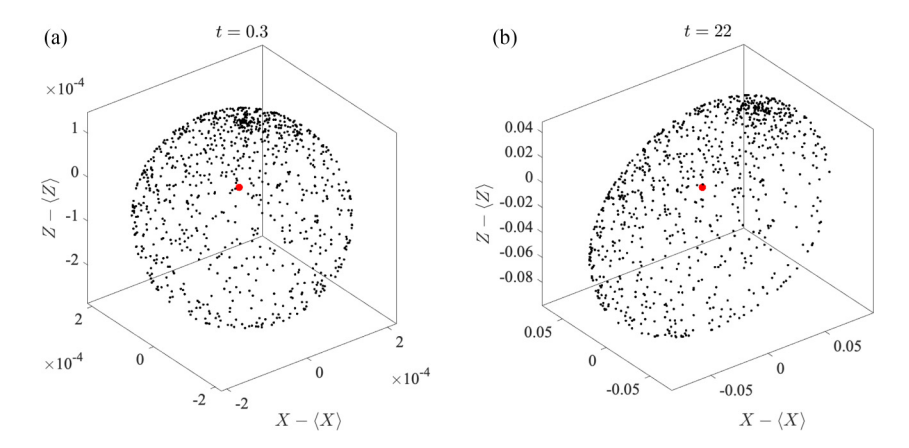


FIG. 9. Particle clouds at different times in a particle dispersion simulation where $\varepsilon_{\rm w}=0.3$, $\lambda=0.6$, and $v_{Z,{\rm isotropic}}=0.05$: (a) initial cloud growth due to isotropic orientation distribution and (b) increased particle dispersion in the wave direction due to Stokes drift shear.

IV. CONCLUSIONS

We have considered the motion of small spheroidal particles within the flow field of small-amplitude progressive waves. By using a multiscale expansion, the wave-averaged motion is isolated from the wave-induced oscillations in particle position and orientation. Analysis of the wave-averaged motion shows that there is a single wave-induced preferential particle orientation for any given particle aspect ratio that is independent of wave parameters. Using a fully 3D analysis, we expand and correct previous results on how oblate and prolate particles align in waves [11,12]; in particular, we find that there are six fixed points in the orientation dynamics (corresponding to three distinct physical orientations) of which only one is stable and that this stable fixed point resides on different branches of solution for oblate and prolate particles. This stable preferential orientation arises due to the differences between the Lagrangian and Eulerian wave averages of the velocity gradients and can thus be considered a Stokes-drift-like correction [Ch. 10, 23].

The stable preferential orientations also induce a horizontal drift in the negative wave direction, opposite the Stokes drift, and a lower settling velocity than random (isotropic) orientations. The horizontal drift opposing the Stokes drift eventually overcomes it as particles settle lower into the water column where the Stokes drift decays.

Wave-averaged particle motion results in particle dispersion due to differences in particle orientations that in turn determine particle drift. For a point cloud of particles released in quiescent water with an initially isotropic distribution of orientations, particle dispersion initially follows a ballistic regime whose coefficient is a function of particle shape, size, and density as given in (16). Waves act to reduce the vertical dispersion by aligning all particles into the same orientation. Waves also act to increase the horizontal dispersion, which results in a (temporary) superballistic horizontal particle cloud growth, but this is caused primarily by the Stokes drift shear acting on the vertical extent of the particle cloud rather than direct effects of particle shape, size, or density. The existence of this superballistic regime may be partly responsible for the observed widespread distributions of anisotropic particles such as microplastics in wavy environments [24]. These results also preserve the idea previously put forward [11] that the horizontal size of the particle cloud is controlled by a combination of settling and alignment, where faster settling particles do not have enough time to be dispersed by Stokes drift shear and slowly settling particles stop dispersing after they reach wave-induced preferential alignment. However, our analysis clarifies the fact that the effect of particle shape is primarily in setting the initial dispersion rate (16) before the effects of wave action becomes important.

Considering the limitations and future extensions of this model, we note that the particle model (4) is valid in the limit of small inertia, and the flow model (1)–(3) is valid in the limit of small amplitude. While the small wave amplitude assumption is not considered too restrictive, it is expected that particle and fluid inertia will begin to influence particle motion for applications such as microplastics and plankton (see, for example, Refs. [25–27] for experimental evidence on inertial effects). Particle inertia, quantified by the Stokes number, tends to be small, especially in field conditions where the wave period is large, and is not expected to alter our results significantly. Fluid inertia around the particle is more likely to be important. In this regard, we have shown that assuming particles settle in their inertial orientation (minimum settling velocity over all orientations) results only in a small error when computing particle drift across a range of particle shapes. Finally, the model here is fully deterministic, and hence particle motion is always a function of its initial conditions. Future work will examine the effects of noise (e.g., turbulence) on particle dynamics to understand how particle orientation, drift, and dispersion are affected.

ACKNOWLEDGMENT

N.P. acknowledges support from the U.S. National Science Foundation (CBET-2211704 and OCE-2048676).

APPENDIX A: PARTICLE SETTLING VECTOR

In the limit of small inertia (small spheroids moving slowly with respect to the background fluid velocity), the particle equation of translation motion is given by

$$0 = -K\boldsymbol{w} - (\rho_{p} - \rho)\frac{\pi}{6} d_{p}^{2} \ell_{p} g \boldsymbol{e}_{z}, \tag{A1}$$

which involves the slip velocity $\mathbf{w} = \mathbf{v} - \mathbf{u}$ as the difference between the particle velocity \mathbf{v} and the fluid velocity \mathbf{u} , the Stokes resistance tensor \mathbf{K} , the particle diameter d_p , the particle length ℓ_p , the particle density ρ_p , the fluid density ρ , and the gravitational acceleration \mathbf{g} , with \mathbf{e}_z being the unit vector pointing opposite to gravity. The force balance is between the drag and buoyancy, with other terms such as particle inertia, added mass, force due to the undisturbed fluid inertia, and the Basset history force all neglected under the assumptions of small inertia. Guazzelli $\mathbf{e}t$ $\mathbf{a}l$. [22] provide a discussion of this physical situation in their Chs. 1–3.

In quiescent fluid, (A1) gives the settling velocity vector

$$\boldsymbol{w} = -(\rho_{\rm p} - \rho) \frac{\pi}{6} d_{\rm p}^2 \ell_{\rm p} g \boldsymbol{K}^{-1} \boldsymbol{e}_z, \tag{A2}$$

where $K = R^T K' R$ with R being the rotation matrix that rotates the laboratory frame into the particle frame and K' being the resistance tensor in the particle frame. For spheroids, K' is a diagonal matrix composed of the resistance coefficient parallel (K'_{\parallel}) and perpendicular (K'_{\perp}) to the particle axis of symmetry. Using $K^{-1} = R^T K'^{-1} R$, it can be shown that

$$\mathbf{K}^{-1}\mathbf{e}_{z} = {K'_{\perp}}^{-1}\mathbf{e}_{z} + ({K'_{\parallel}}^{-1} - {K'_{\perp}}^{-1})(\mathbf{e}_{z} \cdot \mathbf{p})\mathbf{p}. \tag{A3}$$

Substituting (A3) into (A2) gives the spheroid settling velocity vector

$$\boldsymbol{w} = -v_{s\perp}\boldsymbol{e}_z - (v_{s\parallel} - v_{s\perp})(\boldsymbol{e}_z \cdot \boldsymbol{p})\boldsymbol{p},\tag{A4}$$

where $v_{s\perp}$ is the settling velocity for the particle symmetry axis is perpendicular to gravity and $v_{s\parallel}$ is the same for the axis parallel to gravity. The settling has a component purely in the direction of gravity and a component in the direction of the symmetry axis, which in turn can have components both parallel and perpendicular to gravity.

The resistance coefficients in the particle frame have expressions of the form K'_{\perp} , $K'_{\parallel} = 3\pi \rho v d_{\rm p} f({\rm AR})$ where the shape function $f({\rm AR})$ is different for prolate and oblate particles and also different for motion parallel or perpendicular to the particle symmetry axis. Using previously published shape functions ([28], Chs. 5–11), we find the following expressions for the settling velocities:

Prolate (AR > 1):

$$v_{\text{s}\parallel} = \frac{(\rho_{\text{p}} - \rho)d_{\text{p}}\ell_{\text{p}}g}{18\rho\nu} \frac{3}{8} \left[-\frac{2AR}{AR^2 - 1} + \frac{2AR^2 - 1}{(AR^2 - 1)^{3/2}} \ln(\frac{AR + \sqrt{AR^2 - 1}}{AR - \sqrt{AR^2 - 1}}) \right], \quad (A5a)$$

$$v_{s\perp} = \frac{(\rho_{\rm p} - \rho)d_{\rm p}\ell_{\rm p}g}{18\rho\nu} \frac{3}{8} \left[\frac{AR}{AR^2 - 1} + \frac{2AR^2 - 3}{(AR^2 - 1)^{3/2}} \ln(AR + \sqrt{AR^2 - 1}) \right]. \tag{A5b}$$

Oblate (AR < 1):

$$v_{\rm s\parallel} = \frac{(\rho_{\rm p} - \rho)d_{\rm p}\ell_{\rm p}g}{18\rho\nu} \frac{3}{8} \left[\frac{2AR}{1 - AR^2} + \frac{2(1 - 2AR^2)}{(1 - AR^2)^{3/2}} \tan^{-1} \left(\frac{\sqrt{1 - AR^2}}{AR} \right) \right], \tag{A6a}$$

$$v_{s\perp} = \frac{(\rho_{\rm p} - \rho)d_{\rm p}\ell_{\rm p}g}{18\rho\nu} \frac{3}{8} \left[-\frac{AR}{1 - AR^2} - \frac{2AR^2 - 3}{(1 - AR^2)^{3/2}} \sin^{-1}(\sqrt{1 - AR^2}) \right]. \tag{A6b}$$

The settling velocity for a volume-matched sphere is

$$v_{\text{s,sphere}} = \frac{[\rho_{\text{p}} - \rho)(V_{\text{p}}/(\pi/6)]^{2/3}g}{18\rho\nu} = \frac{(\rho_{\text{p}} - \rho)d_{\text{p}}\ell_{\text{p}}g}{18\rho\nu} \,\text{AR}^{-1/3},\tag{A7}$$

where $V_p = (\pi/6)d_p^2 \ell_p$ is the particle volume.

The expressions (A5)–(A7) are made dimensionless by dividing by (ω/k) when used in the main body of the paper.

APPENDIX B: MULTISCALE EXPANSION

The ODEs for particle motion (6) are

$$\dot{x} = \varepsilon_{\rm w} c(z) \cos(x - t) - (v_{\rm sll} - v_{\rm sl}) \cos \phi \sin \phi \sin^2 \theta, \tag{B1a}$$

$$\dot{y} = -(v_{\rm SII} - v_{\rm SI})\cos\phi\cos\theta\sin\theta,\tag{B1b}$$

$$\dot{z} = \varepsilon_{\rm w} \,\mathrm{s}(z) \sin(x-t) - v_{\rm s} + (v_{\rm s} - v_{\rm s}) \cos^2 \phi \,\sin^2 \theta, \tag{B1c}$$

$$\dot{\phi} = \lambda \, \varepsilon_{\rm w} \left[s(z) \cos (x - t) \cos 2\phi - c(z) \sin (x - t) \sin 2\phi \right], \tag{B1d}$$

$$\dot{\theta} = \lambda \, \varepsilon_{\rm w} \left[s(z) \cos (x - t) \sin 2\phi + c(z) \sin (x - t) \cos 2\phi \right] \sin \theta \cos \theta, \tag{B1e}$$

where recall that c(z) and s(z) were defined in (2). We subject these equations to a multiscale expansion, where t is the fast time at which wave-induced oscillations occur and $T = \epsilon^2 t$ is the slow time at which wave-averaged motions occur. Here ϵ is a small quantity that acts as an ordering parameter. The fluid velocity is rescaled as $\varepsilon_w \to \epsilon \varepsilon_w$, and the particle settling velocity is rescaled as $v_s \to \epsilon^2 v_s$. Substituting the expansion and scalings into (B1) gives

$$\partial_t x + \epsilon^2 \partial_T x = \epsilon \, \varepsilon_{\rm w} \, c(z) \cos(x - t) - \epsilon^2 (v_{\rm s} - v_{\rm s}) \cos \phi \sin \phi \sin^2 \theta, \tag{B2a}$$

$$\partial_t y + \epsilon^2 \partial_T y = -\epsilon^2 (v_{\rm sll} - v_{\rm sl}) \cos \phi \cos \theta \sin \theta, \tag{B2b}$$

$$\partial_t z + \epsilon^2 \partial_T z = \epsilon \, \varepsilon_{\rm w} \, {\rm s}(z) \sin(x - t) - \epsilon^2 [v_{\rm s\perp} + (v_{\rm s\parallel} - v_{\rm s\perp}) \cos^2 \phi \sin^2 \theta], \tag{B2c}$$

$$\partial_t \phi + \epsilon^2 \partial_T \phi = \lambda \, \epsilon \varepsilon_{\rm w} \left[s(z) \cos (x - t) \cos 2\phi - c(z) \sin (x - t) \sin 2\phi \right], \tag{B2d}$$

$$\partial_t \theta + \epsilon^2 \partial_T \theta = \lambda \, \epsilon \varepsilon_{\rm w} \left[s(z) \cos \left(x - t \right) \sin 2\phi + c(z) \sin \left(x - t \right) \cos 2\phi \right] \sin \theta \cos \theta. \quad (B2e)$$

At order ϵ^0 , $\partial_t x_0 = \partial_t y_0 = \partial_t z_0 = \partial_t \phi_0 = \partial_t \theta_0 = 0$, showing that the leading order solution is only a function of the slow timescale: $x_0 = X(T)$, $y_0 = Y(T)$, $z_0 = Z(T)$, $\phi_0 = \Phi(T)$, and $\theta_0 = \Theta(T)$.

At order ϵ^1 ,

$$\begin{split} & \partial_t x_1 = \varepsilon_{\mathrm{w}} \, \mathrm{c}(Z) \cos(X-t), \quad \partial_t y_1 = 0, \\ & \partial_t z_1 = \varepsilon_{\mathrm{w}} \, \mathrm{s}(Z) \sin(X-t), \\ & \partial_t \phi_1 = \lambda \, \varepsilon_{\mathrm{w}} \, [\mathrm{s}(Z) \cos(X-t) \cos 2\Phi - \mathrm{c}(Z) \sin(X-t) \sin 2\Phi], \\ & \partial_t \theta_1 = \tfrac{1}{2} \lambda \, \varepsilon_{\mathrm{w}} \sin 2\Theta \, [\mathrm{s}(Z) \cos(X-t) \sin 2\Phi + \mathrm{c}(Z) \sin(X-t) \cos 2\Phi]. \end{split}$$

We integrate with the requirement that the wave-period average $((1/2\pi) \int_0^{2\pi} dt)$ must be zero; this gives the first-order solutions, which are the leading order oscillatory motions at the fast timescale:

$$x_1 = -\varepsilon_{\rm w} \, c(Z) \sin(X - t), \tag{B3a}$$

$$y_1 = 0, (B3b)$$

$$z_1 = \varepsilon_{\rm w} \, {\rm s}(Z) \, {\rm cos}(X - t),$$
 (B3c)

$$\phi_1 = -\lambda \,\varepsilon_{\rm w}[s(Z)\sin{(X-t)}\cos{2\Phi} + c(Z)\cos{(X-t)}\sin{2\Phi}],\tag{B3d}$$

$$\theta_1 = \frac{1}{2}\lambda \,\varepsilon_{\rm w}[c(Z)\cos{(X-t)}\cos{2\Phi} - s(Z)\sin{(X-t)}\sin{2\Phi}]\sin{2\Theta}. \tag{B3e}$$

At order ϵ^2 ,

$$\begin{split} \partial_t x_2 + \partial_T X &= \varepsilon_{\mathrm{w}}[\mathrm{s}(Z)\cos(X-t)z_1 - \mathrm{c}(Z)\sin(X-t)x_1] - (v_{\mathrm{s}\parallel} - v_{\mathrm{s}\perp})\sin\Phi\cos\Phi\sin^2\Theta, \\ \partial_t y_2 + \partial_T Y &= -(v_{\mathrm{s}\parallel} - v_{\mathrm{s}\perp})\cos\Phi\cos\Theta\sin\Theta, \\ \partial_t z_2 + \partial_T Z &= \varepsilon_{\mathrm{w}}[\mathrm{s}(Z)\cos(X-t)x_1 + \mathrm{c}(Z)\sin(X-t)z_1] - [v_{\mathrm{s}\perp} + (v_{\mathrm{s}\parallel} - v_{\mathrm{s}\perp})\cos^2\Phi\sin^2\Theta], \\ \partial_t \phi_2 + \partial_T \Phi &= \lambda \, \varepsilon_{\mathrm{w}}\{\mathrm{s}(Z)[-2\sin2\Phi\cos(X-t)\phi_1 - \sin(X-t)(\sin2\Phi z_1 + \cos2\Phi x_1)] \\ &\quad + \mathrm{c}(Z)[-2\cos2\Phi\sin(X-t)\phi_1 + \cos(X-t)(\cos2\Phi z_1 - \sin2\Phi x_1)]\}, \\ \partial_t \theta_2 + \partial_T \Theta &= \frac{1}{2}\lambda \, \varepsilon_{\mathrm{w}}\{\mathrm{s}(Z)[2\cos(X-t)(\cos2\Theta\sin2\Phi\theta_1 + \sin2\Theta\cos2\Phi\phi_1) \\ &\quad - \sin2\Theta\sin(X-t)(\sin2\Phi x_1 - \cos2\Phi z_1)] + \mathrm{c}(Z)[2\sin(X-t) \\ &\quad (\sin2\Theta\sin2\Phi\phi_1 - \cos2\Theta\cos2\Phi\theta_1) + \sin2\Theta\cos(X-t)(\cos2\Phi x_1 + \sin2\Phi z_1)]\}. \end{split}$$

By substituting (B3) into the above expressions and wave-averaging to remove the fast oscillations, we find the desired wave-averaged particle motion at the slow timescale (7):

$$\partial_T X = \varepsilon_w^2 C(Z) - (v_{s\parallel} - v_{s\perp}) \cos \Phi \sin \Phi \sin^2 \Theta, \tag{B4a}$$

$$\partial_T Y = -(v_{s\parallel} - v_{s\perp})\cos\Phi\sin\Theta\cos\Theta, \tag{B4b}$$

$$\partial_T Z = -[v_{s\perp} + (v_{s\parallel} - v_{s\perp})\cos^2\Phi\sin^2\Theta], \tag{B4c}$$

$$\partial_T \Phi = \lambda \varepsilon_w^2 S(Z)(\lambda + \cos 2\Phi),$$
 (B4d)

$$\partial_T \Theta = \lambda \varepsilon_w^2 S(Z) \sin 2\Phi \sin \Theta \cos \Theta, \tag{B4e}$$

where the functions C(Z) and S(Z) were defined in (8).

To find the second-order solutions, we subtract (B4) from the ϵ^2 equations to get

$$\partial_t x_2 = -\varepsilon_{\mathrm{w}}^2 \frac{\cos 2(X - t)}{2 \cosh^2 kh}, \quad \partial_t y_2 = 0,$$

 $\partial_t z_2 = 0$,

$$\partial_t \phi_2 = -\varepsilon_{\rm w}^2 \mathbf{S}(Z) \lambda^2 \cos 2(X-t) \cos 4\Phi + \lambda^2 \varepsilon_{\rm w}^2 \mathbf{C}(Z) \sin 2(X-t) \sin 4\Phi + \varepsilon_{\rm w}^2 \frac{\sin 2(X-t)}{2 \cosh^2 kh} \sin 2\Phi,$$

$$\begin{split} \partial_t \theta_2 &= \frac{1}{16} \lambda \, \frac{\varepsilon_\mathrm{w}^2}{\cosh^2 kh} \{ \lambda \sin 2(X-t) \sin 4\Theta \left[1 + \cos 4\Theta \cosh 2(Z+kh) \right] \\ &+ 4 \sin 2(X-t) \sin 2\Theta \left[\lambda - \cos 2\Phi - 4 \cos 4\Phi \cosh 2(Z+kh) \right] \} \\ &+ \varepsilon_\mathrm{w}^2 \frac{\sin 2(X-t)}{2 \cosh^2 kh} \sin 2\Phi + \frac{1}{8} \lambda^2 \varepsilon_\mathrm{w}^2 \, \mathrm{C}(Z) \sin 2(X-t) \sin 4\Theta. \end{split}$$

Integrating with the requirement that the wave-period average must be zero gives

$$x_2 = \frac{1}{2} \varepsilon_{\rm w}^2 \frac{\sin 2(X - t)}{2\cosh^2 kh},\tag{B5a}$$

$$y_2 = 0, (B5b)$$

$$z_2 = 0, (B5c)$$

$$\phi_2 = \frac{1}{2}\lambda \frac{\varepsilon_{\rm w}^2}{2\cosh^2 kh} \{\cos 2(X - t)[\lambda \sin 4\Phi \cosh 2(Z + kh) + \sin 2\Phi] + \lambda \cos 4\Phi \sinh 2(Z + kh) \sin 2(X - t)\},$$
(B5d)

$$\theta_2 = \frac{1}{16}\lambda \frac{\varepsilon_{\rm w}^2}{2\cosh^2 kh} \{2\sin 2\Theta\cos 2(X-t)[\lambda(\cos 2\Theta+2) - 2\cos 2\Phi] + \lambda[4\sin 2\Theta - \sin(4\Theta)]$$

$$\times [\sin 4\Phi \sinh 2(Z+kh)\sin 2(X-t) - \cos 4\Phi \cosh 2(Z+kh)\cos 2(X-t)]\}. \tag{B5e}$$

For a given set of initial conditions of the full dynamics, the equivalent initial conditions in the wave-averaged dynamics can be derived by first writing the expansion at t=0 [e.g., $x(0)=X(0)+\epsilon x_1(0)+\epsilon^2 x_2(0)+\cdots$], then substituting in an expansion for the wave-averaged initial condition [e.g., $X(0)=X_0(0)+\epsilon X_1(0)+\epsilon^2 X_2(0)+\cdots$], and finally collecting terms of the same order to find the terms in the wave-averaged initial condition expansion [e.g., $X_1(0), X_2(0)$] in terms of the initial conditions of the full system. Doing so for each variable results in the following projection of the initial conditions of the full system into the wave-averaged system [correct to $O(\epsilon^2)$]:

$$X = x + \varepsilon_{\rm w} c(z) \sin x + \frac{3}{4} \varepsilon_{\rm w}^2 \frac{\sin 2x}{\cosh^2 kh},$$
 (B6a)

$$Y = y, (B6b)$$

$$Z = z - \varepsilon_{\rm w} \,\mathrm{s}(z) \cos x + \frac{1}{2} \varepsilon_{\rm w}^2 \frac{\sinh[2(z+kh)]}{\cosh^2 kh}, \tag{B6c}$$

$$\Phi = \phi + \lambda \frac{\varepsilon_{w}}{\cosh kh} [\cos 2\phi \sin x \sinh(z + kh) + \sin 2\phi \cos x \cosh(z + kh)]$$

$$-\frac{1}{2}\lambda \frac{\varepsilon_{\rm w}^{2}}{2\cosh^{2}kh} \{4\cosh^{2}(z+kh)(\sin 2\phi \sin^{2}x - \lambda \sin 4\phi \cos^{2}x) \\ -\lambda \cos 4\phi \sin 2x \sinh[2(z+kh)] + \lambda \sin 4\phi \{\cosh[2(z+kh)] + \cos 2x - 1\} \\ +\sin 2\phi [4\cos^{2}x \sinh^{2}(z+kh) + \cos 2x]\},$$
 (B6d)

$$\Theta = \theta - \frac{1}{2}\lambda \frac{\varepsilon_{w}}{\cosh kh} \sin 2\theta [\cos 2\phi \cos x \cosh(z + kh) - \sin 2\phi \sin x \sinh(z + kh)]$$

$$+ \frac{1}{32}\lambda \frac{\varepsilon_{w}^{2}}{\cosh^{2}kh} \{\lambda \sin 4\phi \sin 2x \sinh[2(z + kh)](4 \sin 2\theta - \sin 4\theta)$$

$$+ 8 \sinh^{2}(z + kh)[\lambda \sin 4\theta \sin^{2} 2\phi \sin^{2} x + 2 \sin 2\theta \cos 2\phi(2\lambda \cos 2\phi \sin^{2} x + \cos^{2} x)]$$

$$+ 8 \cosh^{2}(z + kh)(4\lambda \sin 2\theta \sin^{2} 2\phi \cos^{2} x + \lambda \sin 4\theta \cos^{2} 2\phi \cos^{2} x + 2 \sin 2\theta \cos 2\phi \sin^{2} x)$$

$$+ \lambda(4 \sin 2\theta - \sin 4\theta) \cos 4\phi \cos 2x \cosh[2(z + kh)] - 2 \sin 2\theta \cos 2x[\lambda(\cos 2\theta + 2)$$

$$-2 \cos 2\phi]\}.$$
(B6e)

where initial conditions are implied [i.e., X = X(0), z = z(0), etc.].

^[1] I. Eames, Settling of particles beneath water waves, J. Phys. Oceanogr. 38, 2846 (2008).

^[2] F. Santamaria, G. Boffetta, M. M. Afonso, A. Mazzino, M. Onorato, and D. Pugliese, Stokes drift for inertial particles transported by water waves, Europhys. Lett. **102**, 14003 (2013).

^[3] M. Bakhoday-Paskyabi, Particle motions beneath irrotational water waves, Ocean Dyn. 65, 1063 (2015).

^[4] M. Bakhoday-Paskyabi, Turbulence-particle interactions under surface gravity waves, Ocean Dyn. 66, 1429 (2016).

^[5] T. S. van den Bremer, C. Whittaker, R. Calvert, A. Raby, and P. H. Taylor, Experimental study of particle trajectories below deep-water surface gravity wave groups, J. Fluid Mech. 879, 168 (2019).

^[6] R. Calvert, C. Whittaker, A. Raby, P. H. Taylor, A. G. L. Borthwick, and T. S. van den Bremer, Laboratory study of the wave-induced mean flow and set-down in unidirectional surface gravity wave packets on finite water depth, Phys. Rev. Fluids 4, 114801 (2019).

^[7] M. H. DiBenedetto, Non-breaking wave effects on buoyant particle distributions, Front. Marine Sci. 7, 148 (2020).

^[8] J. J. Webber and H. E. Huppert, Stokes drift in coral reefs with depth-varying permeability, Philos. Trans. R. Soc. A **378**, 20190531 (2020).

- [9] R. Calvert, M. McAllister, C. Whittaker, A. Raby, A. Borthwick, and T. van den Bremer, A mechanism for the increased wave-induced drift of floating marine litter, J. Fluid Mech. 915, A73 (2021).
- [10] M. H. DiBenedetto, L. K. Clark, and N. Pujara, Enhanced settling and dispersion of inertial particles in surface waves, J. Fluid Mech. 936, A38 (2022).
- [11] M. H. DiBenedetto, N. T. Ouellette, and J. R. Koseff, Transport of anisotropic particles under waves, J. Fluid Mech. 837, 320 (2018).
- [12] M. H. DiBenedetto and N. T. Ouellette, Preferential orientation of spheroidal particles in wavy flow, J. Fluid Mech. 856, 850 (2018).
- [13] M. H. DiBenedetto, J. R. Koseff, and N. T. Ouellette, Orientation dynamics of nonspherical particles under surface gravity waves, Phys. Rev. Fluids 4, 034301 (2019).
- [14] L. K. Clark, M. H. DiBenedetto, N. T. Ouellette, and J. R. Koseff, Settling of inertial nonspherical particles in wavy flow, Phys. Rev. Fluids 5, 124301 (2020).
- [15] L. K. Clark, M. H. DiBenedetto, N. T. Ouellette, and J. R. Koseff, Dispersion of finite-size, non-spherical particles by waves and currents, J. Fluid Mech. **954**, A3 (2023).
- [16] K. Ma, N. Pujara, and J.-L. Thiffeault, Reaching for the surface: Spheroidal microswimmers in surface gravity waves, Phys. Rev. Fluids 7, 014310 (2022).
- [17] M. A. R. Koehl, J. A. Strother, M. A. Reidenbach, J. R. Koseff, and M. G. Hadfield, Individual-based model of larval transport to coral reefs in turbulent, wave-driven flow: Behavioral responses to dissolved settlement inducer, Mar. Ecol.: Prog. Ser. 335, 1 (2007).
- [18] M. A. R. Koehl and M. A. Reidenbach, Swimming by microscopic organisms in ambient water flow, Exp. Fluids 43, 755 (2007).
- [19] H. L. Fuchs and G. P. Gerbi, Seascape-level variation in turbulence- and wave-generated hydrodynamic signals experienced by plankton, Prog. Oceanogr. **141**, 109 (2016).
- [20] F. M. Ventrella, N. Pujara, G. Boffetta, M. Cencini, J. L. Thiffeault, and F. De Lillo, Microswimmer trapping in surface waves with shear, arXiv:2304.14028.
- [21] G. B. Jeffery, The motion of ellipsoidal particles immersed in a viscous fluid, Proc. R. Soc. London A 102, 161 (1922).
- [22] É. Guazzelli, J. F. Morris, and S. Pic, *A Physical Introduction to Suspension Dynamics*, Cambridge Texts in Applied Mathematics (Cambridge University Press, Cambridge, 2011).
- [23] O. Bühler, *Waves and Mean Flows*, Cambridge Monographs on Mechanics (Cambridge University Press, 2009).
- [24] E. van Sebille, S. Aliani, K. L. Law, N. Maximenko, J. M. Alsina, A. Bagaev, M. Bergmann, B. Chapron, I. Chubarenko, A. Cózar *et al.*, The physical oceanography of the transport of floating marine debris, Environ. Res. Lett. 15, 023003 (2020).
- [25] L. Bergougnoux, G. Bouchet, D. Lopez, and É. Guazzelli, The motion of solid spherical particles falling in a cellular flow field at low Stokes number, Phys. Fluids 26, 093302 (2014).
- [26] D. Lopez and É. Guazzelli, Inertial effects on fibers settling in a vortical flow, Phys. Rev. Fluids 2, 024306 (2017).
- [27] S. Agarwal, F. K. Chan, B. Rallabandi, M. Gazzola, and S. Hilgenfeldt, An unrecognized inertial force induced by flow curvature in microfluidics, Proc. Natl. Acad. Sci. USA 118, e2103822118 (2021).
- [28] J. Happel and H. Brenner, Low Reynolds Number Hydrodynamics, with Special Applications to Particulate Media (Martinus Nijhof, 1983).